water

MDPI

Article

Hydrochemical Response of Karst Groundwater to Rapid Urbanization in Xingtai, North China

Rui Wang [1,2,3,4], Xiaohan Li [5,*], Fenggang Dai [1,2,3,4], Zhichao Cai [1,3], Wenbo He [1,3], Lulu Song [1] and Zhoupan Jiang [1]

[1] School of Water Resources and Environment, Hebei GEO University, Shijiazhuang 050031, China; wangrui1116@hgu.edu.cn (R.W.); daifenggang@hgu.edu.cn (F.D.); xscaizhicao@hgu.edu.cn (Z.C.); xshewenbo@hgu.edu.cn (W.H.); xssonglulu@hgu.edu.cn (L.S.); xsjiangzhoupan@hgu.edu.cn (Z.J.)
[2] Hebei Center for Ecological and Environmental Geology Research, Hebei GEO University, Shijiazhuang 050031, China
[3] Hebei Province Key Laboratory of Sustained Utilization and Development of Water Resources, Hebei GEO University, Shijiazhuang 050031, China
[4] Hebei Province Collaborative Innovation Center for Sustainable Utilization of Water Resources and Optimization of Industrial Structure, Hebei GEO University, Shijiazhuang 050031, China
[5] Institute of Hydrogeology and Environmental Geology, Chinese Academy of Geological Sciences, Shijiazhuang 050061, China
* Correspondence: lixiaohan@mail.cgs.gov.cn

Abstract: Karst groundwater is the main water source for domestic, industrial, and agricultural needs in Xingtai City, North China. The objective of this study was to comprehensively access changes in the hydrochemical characteristics and evolution of karst groundwater in response to rapid urbanization. Water samples from the late 2010s and the 1970s were compared utilizing statistical analysis, hydrochemical diagrams, and inverse simulation technology. The total dissolved solids (TDS), total hardness (TH), NO_3^-, and Fe contents were significantly higher in the more recently obtained karst groundwater samples. Further, the dominance of HCO_3-Ca-type water decreased, with new types emerging, relative to 1970s karst groundwater. Abnormal TDS, TH, SO_4^{2-}, NO_3^-, and Cl^- concentrations can be attributed to sewage discharge and fertilizer. Two groundwater discharge areas around the center of Xingtai City and Yangfan Town in the south of the study area were the most significantly affected by human activities. However, inverse modeling indicated that the dissolution of gypsum and halite, as well as cation-exchange processes, occurred in the groundwater paths during both periods. Recent increases in ion concentrations of karst groundwater in the study area have caused carbonate minerals to dissolve, resulting in a further increase of ion concentrations. The hydrochemical response and evolution of karst groundwater requires further study.

Keywords: hydrochemical characteristics; karst groundwater; statistical analysis; PHREEQC inverse modeling; urbanization

Citation: Wang, R.; Li, X.; Dai, F.; Cai, Z.; He, W.; Song, L.; Jiang, Z. Hydrochemical Response of Karst Groundwater to Rapid Urbanization in Xingtai, North China. *Water* **2023**, *15*, 2304. https://doi.org/10.3390/w15122304

Academic Editor: Aldo Fiori

Received: 5 June 2023
Revised: 19 June 2023
Accepted: 19 June 2023
Published: 20 June 2023

1. Introduction

Urbanization is an inevitable trend of the development of human society; it is also a key indicator of the level of industrialization and modernization of a country [1,2]. Currently, 55% of the world's population lives in urban areas, and this percentage is expected to increase to 68% by 2050 [3]. In recent decades, China's social and economic levels have developed rapidly, and the urban population in China has continuously grown, with the urbanization rate increasing from 20.91% in 1982 to 63.22% in 2020 [4]. Thus, China has become a rapidly urbanizing country [5,6].

The formation and prosperity of cities are of great significance for promoting national economic development, strengthening information exchange, and optimizing industrial structures [7–9]. However, the rapid development of cities often leads to a series of

environmental problems [10–12]. Most cities worldwide, especially those in arid and semiarid areas, face challenges caused by the degradation of the water environment [13,14]. The results of previous studies showed that population growth and increasing demand often lead to the overexploitation of water resources, resulting in water shortages and even ecological imbalances [15,16]. The expansion of urban areas leads to less rural farmland and more efficient food production [17]. Thus, the excessive use of fertilizers and pesticides in agricultural areas leads to the deterioration of the soil properties and pollution of rivers and groundwater [18–21]. In addition, many researchers have studied the negative effects of industrial activities on the groundwater quality in urban and peri-urban areas [22,23]. During urbanization in recent decades, the groundwater environment has undergone dramatic changes including a sharp decline in groundwater levels and the degradation of the groundwater quality [24–26].

Groundwater is often the main water source in arid and semiarid areas [27,28]. Therefore, it is important to understand the evolution mechanism of the groundwater environment affected by both natural and human interventions during rapid urbanization, which can provide an essential basis for decision makers to formulate measures that control the deterioration of the groundwater environment. In semiarid environments, achievements in long-term groundwater quantity management and the status quo of the groundwater quality in cities are relatively common [25,29,30], whereas changes in hydrogeochemical laws during urbanization can be easily ignored. Based on previous work, we selected Xingtai, an important node city in the national Beijing–Tianjin–Hebei Province, as a representative medium-sized city with rapid urbanization in the North China Plain. Xingtai City has experienced unparalleled urbanization in recent decades; therefore, karst groundwater in the Baiquan Spring region, which is the only water source for Xingtai's urban water usage, has also undergone significant evolution [31].

The aims of this study were as follows: (1) to analyze the hydrochemical characteristics of karst groundwater during typical periods using summary statistics as well as Piper and Stiff polygon diagrams; (2) to reveal the response of the main chemical components in karst groundwater to rapid urbanization using summary statistics, Piper diagrams, and geographic information system (GIS) techniques; (3) to explore the main human activities that cause water quality deterioration based on multivariate analysis as well as Schoeller and scatter diagrams; and (4) to quantitatively identify the water–rock interactions during urbanization via correlation analysis and hydrogeochemical simulation. These results provide a scientific basis for the protection and sustainable utilization of karst groundwater resources in Xingtai City and other similar semiarid regions.

2. Study Area

Xingtai is in the southern part of the Hebei Province, China and has a continental semiarid monsoon climate. The annual average temperature is 13.1 °C, and the annual average precipitation and potential evaporation are 470.0 and 1702.8 mm, respectively [32]. Precipitation is mainly concentrated from June to September, accounting for ~75% of the annual precipitation. Evaporation is the highest from May to June, accounting for ~33% of the annual total. Xingtai is an important coal and iron energy base in the North China Plain [31]. Its agricultural crops are mainly wheat, corn, millet, peanuts, and cotton, making it one of the production bases for high-quality food and cotton in China [33]. Xingtai's economy has developed rapidly due to its superior natural environmental conditions. In 2020, the city of Xingtai had a population of 7.11 million, of which 3.85 million people lived in urban areas, representing an increase of 1 million compared with the urban population in 2010 [4].

Karst groundwater is the primary water source for domestic, industrial, and agricultural demands in Xingtai City [31]. The study region covers an area of 868 km^2 and lies between 114°10′ and 114°35′ E latitude and 36°56′–37°19′ N longitude (Figure 1). As an independent hydrogeological system, the study area is bounded by groundwater divides in the north and south, water-blocking metamorphic rocks of the Taihang Mountains in the

west, and the Xingtai–Neiqiu and Xingtai–Fengfeng water-blocking faults in the east [34,35]. The topography of the study area varies significantly. The mountainous area in the west has an elevation of ~1000 m and gradually transitions to low mountains and hills with an elevation ranging from 200 to 500 m, whereas the elevation of the plains in the east varies from 60 to 100 m. The rivers that develop from south to north in the study area include the Xiaoma, Baima, Qili, and Sha rivers, which are seasonal rivers originating in the western mountainous area and mainly recharged by atmospheric precipitation.

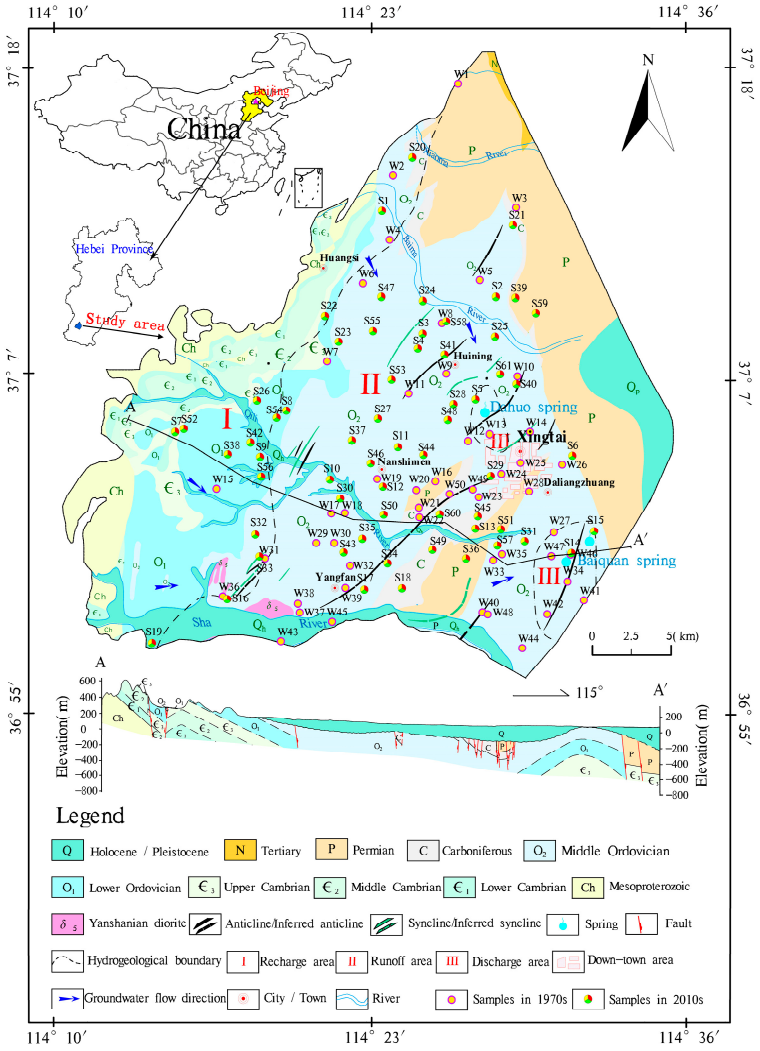

Figure 1. Map showing the location of the study area and sampling sites of karst groundwater.

The strata in the study area, from old to new, include the Changcheng system of the Mesoproterozoic era, Cambrian, and Ordovician systems of the Lower Paleozoic era, Carboniferous and Permian systems of the Upper Paleozoic era, the Triassic system of the Mesozoic era, and the Quaternary system of the Cenozoic era. Mesoproterozoic strata exposed in the west include metamorphic rocks containing calcium and magnesium as well as clastic rocks rich in sulfide [36]. Cambrian and Ordovician strata are exposed to the west of the study area and are covered by Quaternary and Upper Paleozoic strata to the east, with a total thickness ranging from 553 to 826 m [35,37]. The main lithology of the Ordovician is pure limestone, crystalline dolomite, dolomitic limestone, and porphyritic limestone and carbonate rocks are interspersed with layered gypsum, forming gypsum deposits or ores [38,39]. Furthermore, partial boreholes showed that granular halite can also be found in Ordovician limestones and dolomites [37,39].

Large thick Ordovician carbonates with a high permeability and wide distribution area are the main aquifer group in the study area and play a role in gathering and controlling

groundwater flow. Under natural conditions, karst groundwater is recharged by precipitation infiltration and river seepage in the exposed limestone area in the west, converges to the east through the central water-rich area along the terrain, and finally drains to the surface in the form of karst spring water [31,34]. Before the 1980s, karst spring water was discharged within an area exceeding 20 km^2 around Xingtai, which was divided into the Baiquan spring system, led by the Baiquan spring in the southeast of the urban area, and the Dahuo spring system, led by the Dahuo spring in the northwest of the urban area (Figure 1). The two spring systems include 15 spring groups, each consisting of many large and small springs. The average annual flow rate of the Baiquan spring system from 1962 to 1986 was 4.41 m^3/s, and the average annual flow rate of the Dahuo spring system from 1962 to 1980 was 0.87 m^3/s [37].

The exploitation quantity of karst groundwater in the study area gradually increased from 3.40 m^3/s in the early 1980s to 4.74 m^3/s in the early 1990s due to ever-greater demands for industrial, agricultural, and domestic water in Xingtai City, while the Dahuo and Baiquan spring systems stopped flowing in 1981 and 1987, respectively [31,40]. With the acceleration of urbanization from 2001 to 2015, the average exploitation quantity of karst groundwater in the study area reached 6.39 m^3/s, whereas the average recharge of karst groundwater in the study area was only 5.58 m^3/s [31,35,37]. Since the groundwater extraction has been greater than the total recharge of the Ordovician aquifer group for many years, karst water in the study area is in a state of serious overexploitation. As a result, the karst groundwater level in the study area has generally decreased by 60 to 100 m in the past 40 years, with the buried depth of the groundwater level near the Baiquan spring system reaching more than 60 m, which is indicative of considerable damage to the karst groundwater environment [37,41].

3. Methodology

3.1. Sample Collection and Analyses

A total of 61 karst groundwater samples were collected from August 2018 to October 2019 (Figure 1), including 18 samples from a previous study [42] and 43 additional samples from public and private wells in the study area using polyethylene bottles. Groundwater samples were collected and analyzed based on the technical specifications for environmental monitoring of groundwater issued by the Ministry of Environmental Protection of the People's Republic of China (PRC) [43].

Strict quality control was performed during the sampling and analysis. Before sampling, it was necessary to drain the stagnant water in the well and clean the polyethylene bottles three times with flowing groundwater for collection. Sampling was performed within 1 h of cleaning the wells. The temperature and pH values were immediately determined using a portable multi-parameter analyzer (Manta 3.0, Eureka Corporation, Austin, TX, USA) at the sampling site, and the water samples for analyzing metal ion content were acidified with nitric acid to a pH range of 1–2. Immediately after the water samples were collected, the sample bottles were sealed, labeled, stored at 4 °C, and sent to the laboratory for further analysis. Parallel and blank samples were collected and sent to the laboratory together with each batch of water samples. Samples were tested in the Monitoring Center on Groundwater, Mineral Water and Environment, Ministry of Natural Resources. In the laboratory, K^+, Na^+, Ca^{2+}, Mg^{2+}, and Fe were determined via atomic fluorescence spectrometry (ICAP 6300, Thermo Fisher Scientific Inc., Waltham, MA, USA); SO_4^{2-}, Cl^-, NO_3^-, and NO_2^- were determined through ion chromatography (Dionex ICS-90A, Thermo Fisher Scientific Inc., Waltham, MA, USA), and CO_3^{2-} and HCO_3^- were analyzed using acid titration. During the laboratory analysis, standard curves were prepared for atomic fluorescence spectrometry and ion chromatography. The total dissolved solids (TDS) were analyzed with 105 °C dry gravimetry, and the total hardness (TH) was determined through EDTA analysis.

The reliability of the chemical component analysis was tested using the charge balance error percentage (*CBE*%) of the groundwater samples according to the following Equation [43]:

$$CBE\% = \frac{\sum cation - \sum anion}{\sum cation + \sum anion} \times 100\%, \quad (1)$$

where the cations and anions are expressed in milliequivalents per liter (meq/L). When the *CBE*% ranges from −5% to +5%, the water quality analysis results are highly reliable [44]. The results show that the *CBE*% values of the groundwater samples analyzed in this study were all within the threshold. Because of the relatively low concentrations of CO_3^{2-} and NO_2^-, they were not considered in further analyses and discussions.

Based on the previous studies [34,40], the karst groundwater level in the study area followed a periodic change law before 1979, with the supply and discharge volumes remaining balanced for many years. However, after 1979, because of the large-scale exploitation of karst groundwater, the groundwater flow system was affected by human activities, transitioning from a naturally stable state to an unstable state in a natural–artificial composite flow system. Therefore, to better characterize the response of the hydrochemical composition to Xingtai's rapid urbanization in recent decades, the results of the analyses of 50 karst groundwater samples from June 1974 to April 1979 were also collected, including 44 samples from wells and six spring samples. The significant digits of TDS and TH values were the same as those of water samples of 2018–2019, which were both recorded to one decimal place. The significant digits of pH and main ions (except F^- and Fe) of water samples of 1974–1979 were recorded to one decimal place, while the significant digits of these parameters of water samples of 2018–2019 were recorded to two decimal places. In addition, the Fe contents in water samples of 1974–1979 and 2018–2019 were retained to two and three decimal places, respectively. The *CBE*% values of all water samples collected from 1974 to 1979 also passed the data reliability test in Equation (1).

3.2. Statistical Analysis

Statistical analytical methods are effective tools for studying the hydrochemical laws of groundwater. Many researchers have indicated that the influence of the natural environment and human activities on the hydrochemical characteristics of groundwater can be evaluated statistically [13,19,45]. Summary statistics, Pearson's correlation, and cluster analyses were used. Groundwater chemical data were divided into two groups according to different sample collection periods; that is, 1974–1979 (1970s) and 2018–2019 (2010s), with 13 hydrochemical parameters considered in the statistical analysis.

A summary statistical analysis provided a general description of the existing dataset. The minimum, maximum, mean, standard deviation (SD), and coefficient of variation (CV) of the hydrochemical parameters were calculated to reflect the concentration and dispersion trends of the hydrochemical characteristics during the two periods. According to relevant national technical specifications [43], when calculating the average of multiple values with similar accuracy, the number of significant digits can be increased by one. Therefore, in the summary statistical analysis, the significant digits of mean parameter values in the two periods were consistent with those of measured values in the 2010s period, while the SD and CV were retained to two decimal places (excluding Fe). The mean values and SD of Fe concentrations for the two periods were retained to three decimal places to reduce errors.

Pearson's correlation coefficients (r), ranging from −1 to 1, can be used to determine the correlations between various variables. In this study, the significance of the correlation was set to $p < 0.05$. Many research results showed that an r value greater than 0.9 and less than 0.4 indicates a significant strong and weak correlation between the two variables, respectively, whereas an r value range of 0.4–0.7 and 0.7–0.9 indicates a moderate and good correlation between variables, respectively [13,46]. Cluster analysis (CA), another type of multivariate analysis method, has also been frequently used to successfully process and analyze hydrochemical data [45,47,48]. CA is the process of gradually clustering parameters (or samples) into different groups, where parameters (or samples) within the

same group have great similarities, whereas being classified into different groups implies significant differences [45]. In the current study, Pearson's correlation analysis and CA were applied to calculate and analyze the hydrochemical parameters of groundwater samples collected in the 2010s in order to understand the possible sources of ions in groundwater. Summary statistical analysis, correlation analysis, and CA were performed using IBM SPSS Statistics 21.0 [49].

3.3. Graphical Illustration

In this study, concise and easy-to-understand graphical tools were selected to determine the hydrochemical spatiotemporal characteristics of the groundwater samples and facilitate further research. A Piper diagram [50] is a common graphical tool for hydrochemistry consisting of two triangles and a diamond. The triangles on the left and right represent the milliequivalent concentration percentages of the major cations and anions, respectively. The leads of the points plotted on the two triangles intersect the upper diamond and the different zones represent different chemical characteristics [50]. On the other hand, the Stiff polygon diagram [51] is a graphical tool used to visually represent the milliequivalent concentrations of major anions and cations at each sampling point. In this study, Stiff polygon diagrams were combined with sampling locations to analyze the spatial evolution of major ion concentrations. The hydrochemical diagrams drawn in the study were realized using Aquachem 5.1 (Waterloo Hydrogeologic Inc., Waterloo, Canada), a software for hydrochemistry.

In addition, the Kriging interpolation method, which is one of the widely used geostatistical interpolation methods [52,53], was applied to interpolate the concentrations of hydrochemical parameters. In this study, contour maps of the increases in the concentrations of major hydrochemical parameters over the past decades were calculated using the Kriging interpolation method in MapGIS 6.7 (Zondy Cyber S&T., Wuhan, China).

3.4. Inverse Hydrogeochemical Modeling

Saturation index. The saturation index (SI) is an important and widely used indicator in hydrogeochemistry. It can be used to analyze the dissolution and precipitation trends of minerals in groundwater [54,55]. The SI of a mineral in groundwater is defined as follows:

$$SI = \lg \frac{IAP}{K}, \tag{2}$$

where IAP is the product of the ionic activity of the mineral in groundwater, and K is the equilibrium constant of the mineral at a certain temperature. When the SI is equal to 0 ($SI = 0$), the mineral is in an equilibrium state in aqueous solution, whereas $SI < 0$ and $SI > 0$ indicate that the mineral is in a dissolved and precipitated state in aqueous solution, respectively. The SI of minerals was calculated using inverse hydrogeochemical modeling and PHREEQC 3.5.0 (US Geological Survey, Denver, CO, USA).

Inverse hydrogeochemical model. Inverse hydrogeochemical models are also called mass balance models. Based on the analysis of hydrochemical composition at the start and end points of a certain groundwater flow path, hydrogeochemical reactions along the flow path can be inferred using the mass balance model, and the quantity of mass transfer occurring along the path can be quantitatively calculated, revealing the main factors affecting the evolution of groundwater chemical composition [55]. This modeling process can be expressed by the following equation:

$$W_i + P_r = W_f + P_p, \tag{3}$$

where W_i represents initial hydrochemical components at the beginning of the path W_f; represents final hydrochemical components at the end of the path; and P_r and P_p represent the components entering and leaving the aqueous solution during the hydrochemical reaction processes, respectively, which could be gas, minerals, or ion exchange, collectively

referred to as the mineral phase. The abovementioned equation can also be written as a mass conservation equation [55]:

$$\left\{ \sum_{n=1}^{P} \alpha_n b_{n,k} = \Delta m_{T,k} \right\}_{k=1\Lambda j, n=1\Lambda P,} \quad (4)$$

where P is the total number of reactive and generated mineral phases in the reaction; j is the number of elements in the model; α_n is the molar mass of the mineral phase n leaving or entering the solution; $b_{n,k}$ is the stoichiometric coefficient of the element k in the mineral phase n; Δ is the difference between the initial and final values in the reaction; and $m_{T,k}$ is the total molar concentration of the element k in the solution.

Because the number of elements considered in an inverse hydrogeochemical model is often less than the number of mineral phases, the model may have multiple solutions. Therefore, it is necessary to combine relevant research results, such as the mineral composition, state of dissolution or precipitation of minerals, groundwater burial characteristics, and the hydrogeochemical evolution law of the study area to select simulation results consistent with the actual conditions and to improve the reliability of the inverse hydrogeochemical model [48]. Based on the abovementioned principles, an inverse hydrogeochemical model of multiple paths in the two periods was constructed using PHREEQC 3.5.0 (US Geological Survey, Denver, CO, USA).

4. Results and Discussion

4.1. Statistical Analysis of Hydrochemical Components

The summary statistics of the main hydrochemical components were calculated for the two periods, as shown in Table 1.

Table 1. Summary statistics of the main hydrochemical components in karst groundwater for the two periods [1].

Parameter	Samples in 2018–2019 (2010s)					Samples in 1974–1979 (1970s)					WHO Limits	PRC Limits
	Min	Max	Mean	SD	VC (%)	Min	Max	Mean	SD	VC (%)		
pH	7.67	8.47	7.96	0.15	1.92	7.1	8.1	7.57	0.24	3.19	-	6.5–8.5
TDS (mg/L)	227.7	675.1	373.9	100.35	26.84	167.0	382.0	255.9	53.66	20.97	-	1000
TH (mg/L)	183.0	481.9	281.4	71.16	25.29	128.6	294.6	190.7	36.56	19.17	-	450
K^+ (mg/L)	0.53	6.71	1.67	0.91	54.50	0.2	3.9	1.45	0.81	55.86	-	-
Na^+ (mg/L)	7.62	64.58	18.82	9.91	52.66	4.2	33.7	11.96	5.78	48.33	-	200
Ca^{2+} (mg/L)	51.08	145.80	76.92	21.18	27.53	29.7	90.0	53.71	11.46	21.34	-	-
Mg^{2+} (mg/L)	10.30	37.76	21.46	6.01	28.03	7.8	27.2	13.70	3.71	27.10	-	-
Cl^- (mg/L)	8.63	98.33	31.12	21.27	68.35	7.1	41.0	13.47	6.72	49.94	-	250
SO_4^{2-} (mg/L)	15.68	177.80	63.84	36.33	56.91	7.7	98.1	23.70	18.02	76.06	-	250
HCO_3^- (mg/L)	149.18	333.50	227.86	40.62	17.83	151.0	293.0	208.47	30.46	14.61	-	-
NO_3^- (mg/L)	10.76	105.40	30.82	18.29	59.33	0.1	24.0	5.39	4.24	78.72	50	88.6
F^- (mg/L)	0.30	0.69	0.45	0.09	19.66	0.00	0.65	0.29	0.15	52.07	1.5	1.0
Fe (mg/L)	0.005	4.483	0.476	0.783	164.63	0.00	0.03	0.002	0.005	271.00	-	0.3

Note(s): [1] Min, Max, SD, and VC refer to minimum, maximum, standard deviation, and coefficient of variation, respectively.

Compared with the 1970s, the contents of the main hydrochemical parameters in karst groundwater in the study area have increased to varying degrees in recent years. The pH values varied from 7.1 to 8.1 and 7.67 to 8.47 during the 1970s and 2010s, with an average of 7.57 and 7.96, respectively. This indicates that the karst groundwater in the study area was slightly alkaline and that the alkalinity slightly increased overall. During the 1970s, the range of TDS was 167.0–382.0 mg/L in the study area. However, it was 227.7–675.1 mg/L in recent years, and the mean value increased from 255.9 mg/L in the 1970s to 373.9 mg/L in the 2010s. Groundwater samples with TDS values below 1000 mg/L can be classified as freshwater [56]. Therefore, the statistical results indicate that there has been a significant increase in the values over the past few decades. However, the karst groundwater in the study area has always been freshwater. According to the classification of groundwater based on TH [57], the water samples from the 2010s contained no soft

water (<50 mg/L), whereas the proportions of slightly hard water (150 to 300 mg/L), hard water (300 to 450 mg/L), and very hard water (more than 450 mg/L) samples were 65.57, 31.15, and 3.28%, respectively. In addition, the TH value of very hard water exceeded the limit (450 mg/L) of the PRC National Standard [58], indicating that it is not suitable for use as drinking water without proper treatment [57]. In contrast, only soft and slightly hard water samples were collected during the 1970s (Table 1). The statistical results show that the TH of karst groundwater in the study area significantly increased in recent decades.

As shown in Table 1, the statistical results of the major anions (Ca^{2+}, Mg^{2+}, Na^{+}, and K^{+}) and cations (Cl^{-}, $SO_4{}^{2-}$, and $HCO_3{}^{-}$) in the two periods were similar. Among the major cations, the variation coefficients of Ca^{2+} and Mg^{2+} were relatively small, reflecting the relative stability of their concentrations in karst groundwater. Among the major anions, $HCO_3{}^{-}$ had the highest mean value and lowest variation coefficient, indicating that its concentration in groundwater was relatively high and stable. Thus, $HCO_3{}^{-}$ was the main anion in karst water in the study area. In addition, the variation coefficients of Na^{+}, K^{+}, Cl^{-}, and $SO_4{}^{2-}$ in both periods were relatively large, reflecting their significant spatial concentration differences and sensitivity to environmental factors. However, compared with the statistical values for the 1970s, the average concentrations of Cl^{-} and $SO_4{}^{2-}$ doubled in 40 years, from 13.47 and 23.70 mg/L to 31.12 and 63.84 mg/L, respectively.

Among the other main components in Table 1, the maximum value of F^{-} in the water samples taken from 2018 to 2019 was 0.69 mg/L, which is lower than the value for drinking water (1.5 mg/L) recommended by the World Health Organization (WHO) [59]. The minimum value of F^{-} was 0.30 mg/L and the variation coefficient was lower than that of the 1970s period, indicating that F^{-} is widely present in karst groundwater in recent years, with a little difference in the concentration. In the water samples collected during the 1970s, the $NO_3{}^{-}$ and Fe concentrations did not exceed the relevant standards. However, in the samples of the 2010s period, the maximum value of $NO_3{}^{-}$ (105.40 mg/L) exceeded the WHO guideline value (50 mg/L) [59] and the limit value (88.6 mg/L) of the PRC National Standard [58]. In addition, the mean value of Fe (0.476 mg/L) also exceeded the limit value (0.3 mg/L) of the PRC National Standard [58], with an over-limit ratio of 39.3% and a variation coefficient of 164.43% (Table 1). These statistics show that the phenomenon of Fe and $NO_3{}^{-}$ exceeding the limits is noteworthy and that the concentration distribution of Fe exhibits notable regional differences.

4.2. Evolution of Hydrochemical Types

A Piper diagram is an effective and simple graphical method for determining the type and hydrochemical evolution of groundwater [46]. The main ion analysis results of the water samples from the two periods were plotted in a Piper diagram, and a regional Stiff polygon distribution diagram for the 2010s period was drawn to jointly analyze the evolution characteristics of the hydrochemical types, as shown in Figures 2 and 3. The major anions and cations of the water samples shown in Figure 2 are expressed as milliequivalent concentration percentages.

To meet the needs of urban development, large-scale utilization of karst groundwater in the study area began in the 1980s [31,37]. Figure 2 shows that the milliequivalent concentration percentage ranges of Ca^{2+} and Mg^{2+} in most water samples before the 1980s were 50–75% and 15–30%, respectively, and the hydrochemical types were HCO_3-Ca and HCO_3-Ca·Mg types on the whole. Only the relative contents of Mg^{2+} or $SO_4{}^{2-}$ in a few water samples were slightly higher, with HCO_3-Mg·Ca and HCO_3·SO_4-Ca·Mg types forming, respectively. In contrast, the relative contents of Cl^{-} and $SO_4{}^{2-}$ in the water samples collected in recent years significantly increased, and the percentage ranges of Ca^{2+} and Mg^{2+} changed to 45–70% and 15–40%, respectively, which resulted in a significant reduction of HCO_3-Ca-type water and the appearance of SO_4·HCO_3-Ca·Mg, HCO_3·Cl-Ca·Mg, HCO_3·Cl·SO_4-Ca·Mg, and HCO_3·SO_4-Ca types, indicating the complexity of the hydrochemical components.

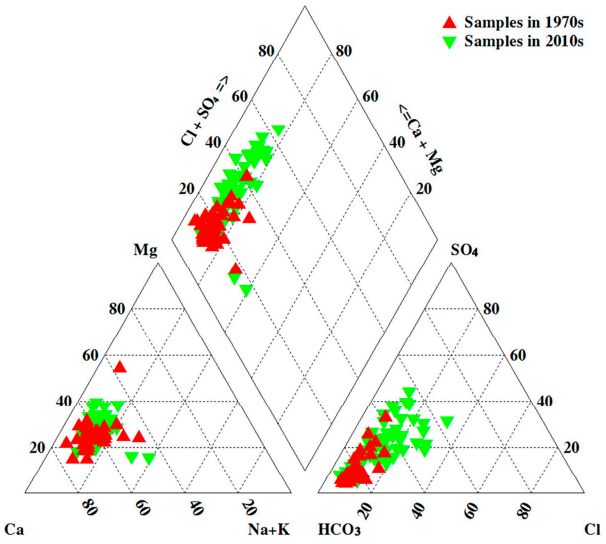

Figure 2. Piper diagram of karst groundwater samples from the two periods.

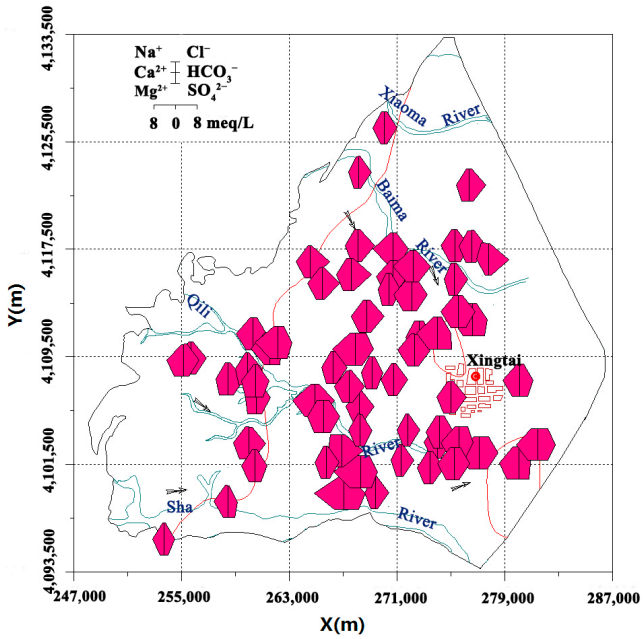

Figure 3. Stiff polygon distribution diagram of karst groundwater samples during the 2010s.

Based on the Stiff polygon distribution diagram (Figure 3), complex hydrochemical types are mainly distributed in natural groundwater discharge areas around downtown Xingtai. The discharge areas are not only densely populated but also low relief areas, where years of continuous overexploitation have further reduced karst groundwater levels [31,40]. The non-equilibrium hydraulic gradient caused by overexploitation of groundwater can lead to inferior water intrusion as well as accumulation of agricultural irrigation and domestic drainage in the region, thus worsening the groundwater quality and complicating hydrochemical compositions [13,20,48]. Therefore, on the north side of the downtown area, that is, near the discharge area of the original Dahuo spring system, the milliequivalent concentration of SO_4^{2-} in some water samples significantly increased, forming the SO_4·HCO_3-Ca·Mg and HCO_3·SO_4-Ca·Mg types. In contrast, the south side of Xingtai's downtown area, near the discharge area of the original Baiquan spring system, was characterized by a moderate increase in the milliequivalent concentration of Cl^- as well as the formation of HCO_3·Cl-Ca·Mg- and HCO_3·Cl·SO_4-Ca·Mg-type water. In a runoff area located in the middle between the Qili and Sha rivers in the central-south of the study

area, the milliequivalent concentrations of main ions in two water samples significantly increased, and HCO_3·SO_4-Ca-type water formed. In contrast, the milliequivalent concentrations of most samples in the recharge area located in the western part of the study area were relatively low, and HCO_3-Ca·Mg-type water was dominant.

4.3. Correlations

Pearson's correlation coefficient (r) can be used to evaluate the strength of the linear correlation between the hydrochemical parameters, as shown in Table 2. The significance level of the correlation is less than 0.05. TDS has a strong correlation coefficient with Ca^{2+} (r = 0.942) and good or moderate correlations with other major ions; that is, SO_4^{2-} (0.804), Cl^- (0.784), Mg^{2+} (0.735), NO_3^- (0.673), Na^+ (0.641), and HCO_3^- (0.512), indicating a significant contribution of these ions to the groundwater composition. In addition, the correlation coefficient between TH and Ca^{2+} reaches 0.961, indicating that Ca^{2+} has the highest contribution to groundwater hardness. Note that a moderate correlation was observed between TH and NO_3^- (r = 0.603). According to Maghrebi et al. (2021) [20], agricultural activities, such as the use of fertilizers, can severely affect groundwater quality. NO_3^- is often used to identify the effects of human agricultural activities on groundwater, with the increase in the NO_3^- content suggesting a considerable shift in hydrochemical compositions [60,61]. Shukla et al. (2021) [62] reported that sewage discharge and agricultural activities may also be sources of increased TDS and TH values. Therefore, the strong correlation between TDS and TH as well as their moderate correlations with NO_3^- suggest that anthropogenic activities have had a certain impact on the groundwater quality.

Table 2. Correlation matrix for measured hydrochemical parameters.

	pH	**TH**	**TDS**	**K^+**	**Na^+**	**Ca^{2+}**	**Mg^{2+}**	**Cl^-**	**SO_4^{2-}**	**HCO_3^-**	**NO_3^-**	**F^-**	**Fe**
pH	1.000	−0.068	−0.041	0.070	0.145	−0.053	−0.075	0.147	−0.122	−0.038	−0.158	−0.008	−0.229
TH		1.000	0.959	0.216	0.425	0.961	0.811	0.774	0.822	0.452	0.603	−0.098	0.017
TDS			1.000	0.216	0.641	0.942	0.735	0.784	0.804	0.512	0.673	−0.121	−0.005
K^+				1.000	0.104	0.202	0.195	0.360	0.371	−0.137	−0.151	0.162	−0.126
Na^+					1.000	0.443	0.271	0.651	0.285	0.547	0.411	−0.149	−0.148
Ca^{2+}						1.000	0.620	0.722	0.811	0.466	0.574	−0.041	−0.022
Mg^{2+}							1.000	0.676	0.622	0.298	0.506	−0.199	0.097
Cl^-								1.000	0.560	0.203	0.417	−0.097	−0.090
SO_4^{2-}									1.000	0.075	0.401	−0.058	0.009
HCO_3^-										1.000	0.284	−0.076	−0.080
NO_3^-											1.000	−0.167	0.228
F^-												1.000	−0.108
Fe													1.000

To further verify the correlations between hydrochemical parameters, several hydrochemical indicators with significant content changes in recent decades, including TDS, TH, SO_4^{2-}, Cl^-, NO_3^-, and Fe, were selected to draw the contour maps of concentration increments, as shown in Figure 4. Compared with the groundwater in the 1970s, the concentration of NO_3^- increased throughout the study area (Figure 4e). Two high-value areas were observed, near Yangfan Town in the south and Huining Town in the north, indicating that human agricultural activities have affected the karst groundwater quality throughout the region, even leading to the concentration of NO_3^- exceeding the standards. In addition, the TDS, TH, and SO_4^{2-} concentrations in these two high-value areas also significantly increased (Figure 4a–c). The high similarity of spatial variation characteristics and good Pearson's correlation coefficients show that diversified anthropogenic sources (e.g., fertilizer and urban sewage) have jointly affected the groundwater during the urbanization of Xingtai over the past few decades, resulting in abnormal contents of multiple ions and comprehensive indicators in the groundwater.

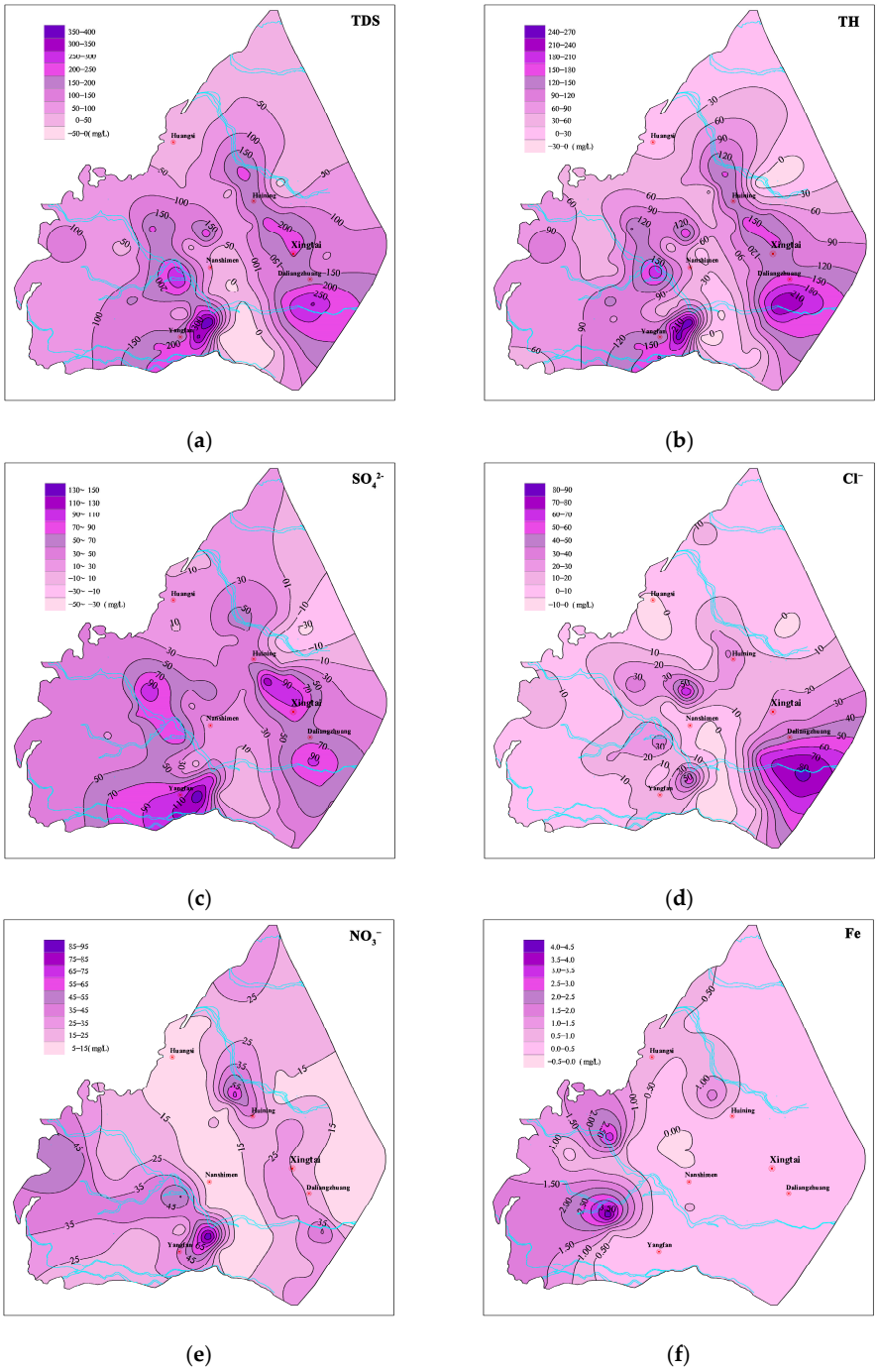

Figure 4. Content increment contour map of hydrochemical indicators in the study area. (**a**) TDS; (**b**) TH; (**c**) SO_4^{2-}; (**d**) Cl^-; (**e**) NO_3^-; (**f**) Fe.

The results in Table 2 indicate a good correlation between Ca^{2+} and SO_4^{2-} (r = 0.811) and a moderate positive correlation between Na^+ and Cl^- (r = 0.651), suggesting the dissolution of sulfate and halite minerals during the flow of karst groundwater [47,63]. The Stiff polygon diagram shows that the concentration of Cl^- increases near the discharge area on the south side of Xingtai's downtown area, with a significant increase in the Cl^- concentration in this area when compared with 40 years ago (Figure 4d). Based on the results of previous studies [20,46,64], seawater intrusion, the evaporation process, and domestic sewage discharge may also increase the Cl^- concentration, in addition to the dissolution of halite. Based on research into the lithology and hydrogeochemical processes within the study area [31,34,39], the evaporation near the discharge areas is weak because

of the evident decline in the groundwater level over the past 40 years. Further, the content of chlorine-bearing minerals in Cambrian and Ordovician strata is not rich. However, as shown in the sectional drawing of Figure 1, the overlying Quaternary strata of karst water sample S14 with a Cl^- concentration of 94.54 mg/L collected in this discharge area are missing, making karst groundwater susceptible to human activities. Therefore, the significant increase in Cl^- concentrations in this area also indicates that anthropogenic sources (e.g., domestic sewage) should be considered.

4.4. Sample Clustering

Cluster analysis was conducted on 61 groundwater samples collected during the 2010s. Ward's method in SPSS version 21.0 [49] was applied to analyze the linkages between groups and the square Euclidean distance was selected as the similarity measure [65,66]. The dendrogram obtained from the cluster analysis is shown in Figure 5. Herein, a linkage distance of 5 was selected, and three groups (Groups 1–3) were clustered. In addition, based on the mean ion concentrations in the groundwater samples from different clustering groups, a Schoeller diagram [67] (Figure 6) and a scatter diagram [68] (Figure 7) were plotted. Figure 6 shows the mean ion concentrations in each group, and Figure 7 reflects the impact of human activities through the Na^+ normalized Cl^- versus $NO_3{}^-$.

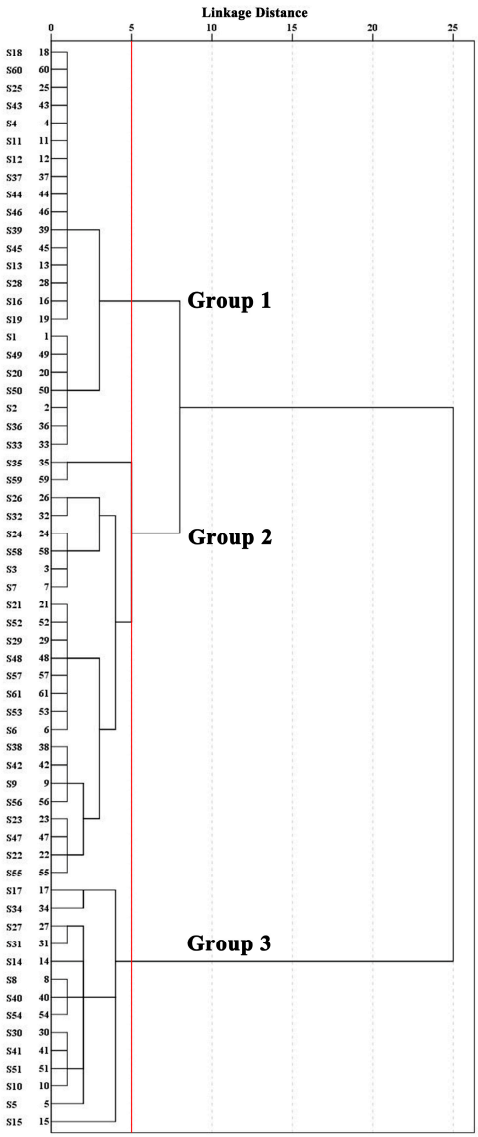

Figure 5. Dendrogram showing the clustering results.

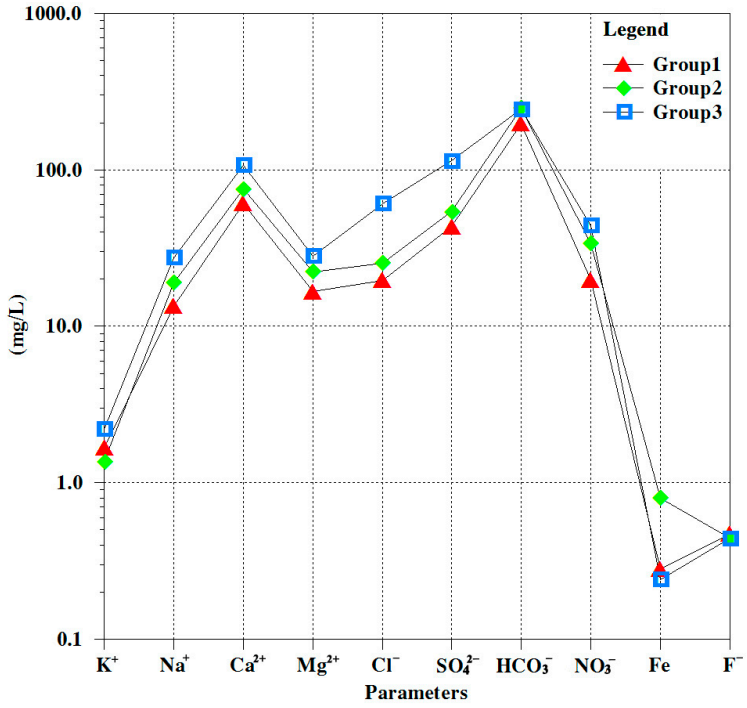

Figure 6. Schoeller diagram of the mean ion concentrations in each group.

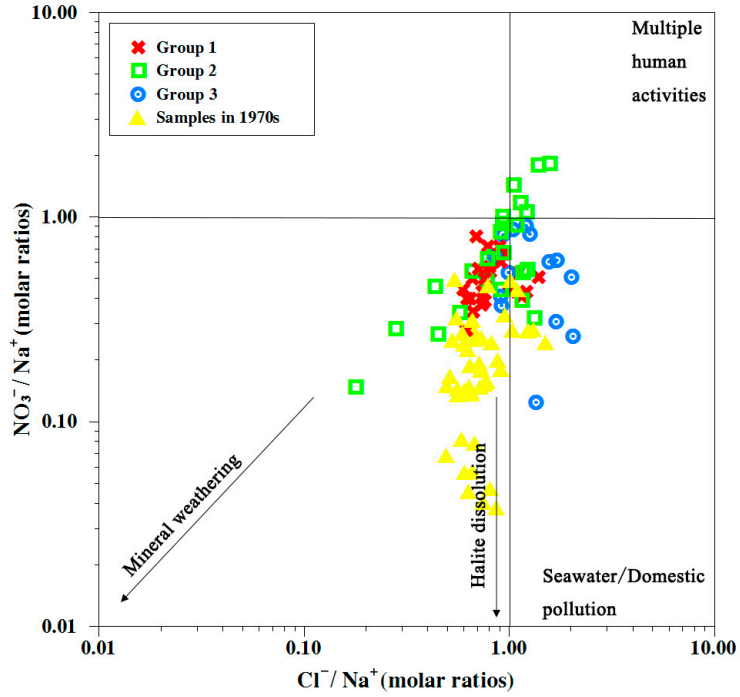

Figure 7. Scatter diagram of Cl^-/Na^+ versus NO_3^-/Na^+ for groundwater samples.

The water samples in Group 1 were mainly taken from the recharge areas to the north (S20 and S1) and south (S19, S16, and S33) of the study area as well as from most runoff areas in the central and southern regions, showing relatively low concentrations of each ion (Figure 6). Figure 7 shows that most of the water samples from Group 1 and the 1970s do not fall into areas significantly affected by human activities. Samples in Group 2 were mainly concentrated in two areas: the northern runoff area and western recharge area near the upper reaches of the Qili River. The mean concentrations of Na^+, Ca^{2+}, Mg^{2+}, Cl^-, SO_4^{2-}, NO_3^-, HCO_3^-, and Fe increased compared to those of Group 1, with NO_3^- and

Fe increasing the most (Figures 6 and 7), which suggests a greater influence of human activities [60,63]. In addition, Figure 5 shows a large linkage distance between Group 3 and the first two groups. Samples (S5, S14, S15, S31, S40, and S51) collected near the discharge areas on the north and south sides of Xingtai's downtown area were clustered into Group 3. Their main anion and cation contents continuously increased, especially the concentrations of Cl^- and SO_4^{2-} (Figure 6). According to previous studies, the discharge of untreated sewage may be a dire threat to the quality of groundwater [20]. As shown in Figure 7, most of the water samples in Group 3 fall in the area of seawater/domestic pollution, indicating their similar sources and hydrochemical evolution processes.

Note that samples S7, S9, S26, S32, S38, S42, S52, and S56 from the westernmost part of the study area were clustered together in Group 2, showing significant differences in the composition of groundwater, such as higher SO_4^{2-} concentrations (Figure 4c) and significantly increased Fe concentrations (Figure 4f) over the past few decades, compared with samples from other recharge areas and downstream runoff areas. The TDS value and SO_4^{2-} concentration of W15, the only groundwater sample collected in the nearby region during the 1970s (Figure 1), were 302.0 and 28.8 mg/L, respectively. As these were higher than their respective mean values (Table 1) of the whole study area at that time, it is necessary to consider the effect of the original environment as well as the influence of human activities through the decades. First, these water samples were relatively concentrated in the carbonate-exposed areas where the karst groundwater is recharged by precipitation infiltration and seepage of the Qili River. According to previous research [69], the solute concentrations of monsoon rivers are highly controlled by changing seasonal hydrological conditions. Therefore, the impact of local hydrological conditions on the compositions of karst groundwater cannot be ignored. Meanwhile, according to previous hydrogeological investigations [36], Mesoproterozoic strata in the westernmost part of the study area contain sulfide-rich clastic rocks that can be oxidized to form SO_4^{2-} and enter groundwater. Further, the Cambrian system is in unconformable contact with underlying Mesoproterozoic strata. Therefore, karst groundwater in the carbonate-exposed area on the western side of the study area may also be affected by the mixing of fissure water in the mountainous bedrock area.

4.5. Inverse Hydrogeochemical Modeling

4.5.1. Determination of Simulation Paths

The reverse hydrogeochemical simulation path must follow the principle that the start and end points are on the same flow path and reflect the changes in the hydrogeochemical characteristics on the flow path while minimizing the effect of sewage discharge on the spatial distribution of ions [48,70].To specifically analyze water-rock interactions of karst aquifers in different development periods, two groundwater flow paths were selected to simulate hydrogeochemical processes in the 2010s based on geological structure, karst groundwater flow field, hydrochemical characteristics, and human activities (Figure 8). Anthropogenic sources have no significant impact on the start and end points selected for the paths, and the simulation paths chosen should also try not to pass through water samples with abnormal ion concentrations, so as to increase the rationality of simulation models in this study. Path I started from the recharge area in the northwest and ended near the discharge area of the Dahuo spring system (S1–S28). Path II started from the recharge area in the southwest and ended near the discharge area of the Baiquan spring system (S33–S57). For comparison, groundwater flow paths I′ and II′ during the 1970s were located close to the two aforementioned paths, as shown in Figure 8.

4.5.2. Determination of Mineral Phases

The determination of mineral phases is key to establishing a reverse hydrogeochemical simulation model, which must be in accordance with the mineral composition of the water-bearing media, the hydrochemical composition of the start and end points of the simulation path, as well as with the related hydrogeochemical processes [55]. In the study area, large thick carbonate rocks are widely distributed, which are mainly composed of

limestone and dolomite and contain abundant karst groundwater. Middle Ordovician carbonate rocks are often interspersed with layered gypsum, and granular halite can also be found in Ordovician limestones and dolomites [38,39]. In addition, Quaternary loose sediments cover carbonate rocks in the central and eastern parts of the study area, and sparse contours of the water table indicate the slowing of the groundwater flow near the discharge area (Figure 8). Therefore, an increase in fine soil particles could promote the cation exchange between groundwater and soil, which could affect the migration and distribution of Ca^{2+}, Mg^{2+}, and Na^{+} in the groundwater [70]. Furthermore, considering that CO_2 is required for both dissolution and precipitation of carbonate rocks [71,72], gas-phase CO_2 was defined as the mineral phase. Therefore, calcite ($CaCO_3$), dolomite ($CaMg(CO_3)_2$), gypsum ($CaSO_4 \cdot nH_2O$), halite (NaCl), CO_2(g), Ca^{2+} exchange (CaX_2), Mg^{2+} exchange (MgX_2), and Na^{+} exchange (NaX) were selected as potential mineral phases participating in the reactions in karst groundwater. The mineral phases were set using the phreeqc.dat database of PHREEQC software.

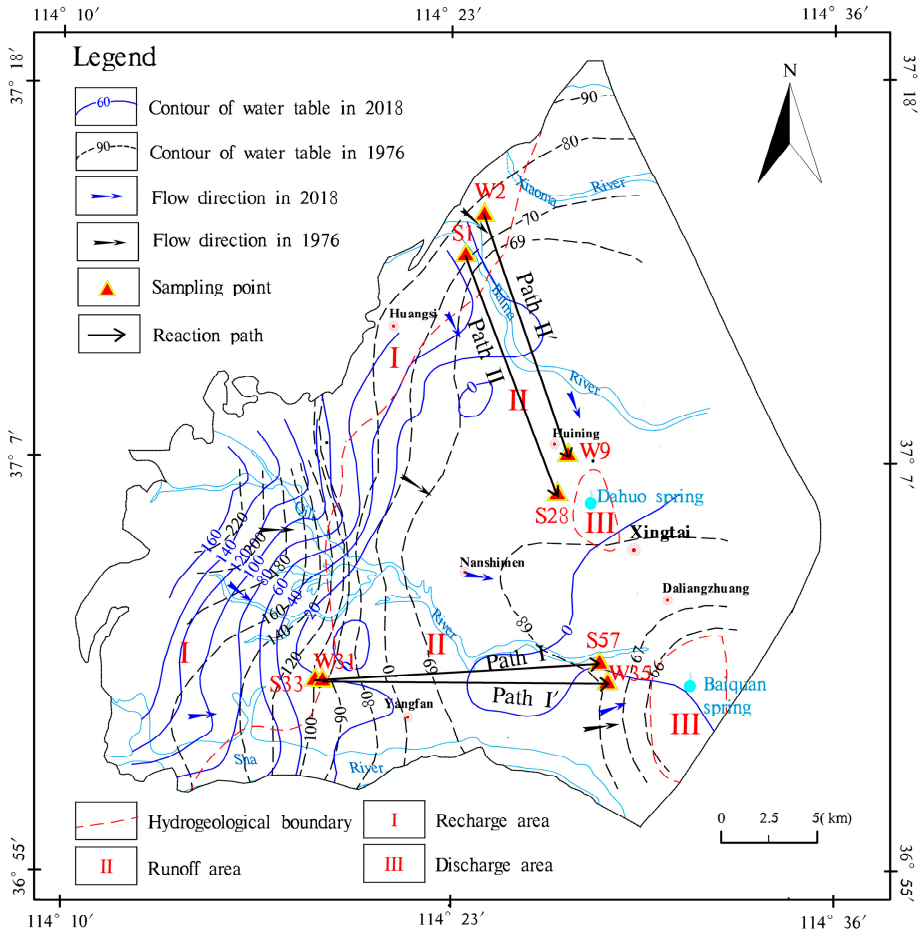

Figure 8. Hydrochemical simulation paths of karst groundwater in the study area.

4.5.3. Simulation Results Analysis

The saturation indices of certain mineral phases at the start and end points of the simulated paths are shown in Table 3. The inverse hydrogeochemical model of each simulation path of karst groundwater was established using PHREEQC software, and the simulation results were appropriately reduced by adjusting the uncertainty. The molar amounts of the transferred minerals are listed in Table 4.

Table 3. Mineral saturation index of the start and end points in the simulated paths.

Title 1	Title 2	Saturation Index of Mineral Phase				
		Calcite	Dolomite	Gypsum	Halite	CO_2 (g)
Path I	Start point (S1)	0.59	0.84	−2.30	−8.30	−3.00
	End point (S28)	0.39	0.48	−1.81	−7.62	−2.68
Path II	Start point (S33)	0.44	0.49	−1.63	−8.20	−2.80
	End point (S57)	0.39	0.44	−1.58	−7.63	−2.46
Path I′	Start point (W2)	0.14	−0.32	−2.53	−8.32	−2.33
	End point (W9)	0.01	−0.31	−2.30	−8.30	−2.23
Path II′	Start point (W31)	−0.27	−0.88	−2.60	−8.73	−2.21
	End point (W35)	0.06	−0.10	−2.21	−8.58	−2.21

Table 4. Results of inverse hydrogeochemical modeling.

Mineral Phase	Calcite	Dolomite	Gypsum	Halite	CO_2 (g)	Ca^{2+} Exchange	Mg^{2+} Exchange	Na^{+} Exchange
Formula	$CaCO_3$	$CaMg(CO_3)_2$	$CaSO_4$	NaCl	CO_2	CaX_2	MgX_2	NaX
Molar amounts of the transferred minerals (mol/L)								
Path I (S1–S28)								
Model 1		2.422×10^{-5}	4.285×10^{-4}	7.283×10^{-4}	8.224×10^{-5}	-7.777×10^{-5}	2.210×10^{-4}	-2.864×10^{-4}
Model 2	-1.555×10^{-4}	1.020×10^{-4}	4.285×10^{-4}	7.283×10^{-4}			1.432×10^{-4}	-2.864×10^{-4}
Model 3	4.844×10^{-5}		4.285×10^{-4}	7.283×10^{-4}		-1.020×10^{-4}	2.452×10^{-4}	-2.864×10^{-4}
Path II (S33–S57)								
Model 1		2.206×10^{-4}	3.068×10^{-6}	6.841×10^{-4}	5.322×10^{-4}	1.340×10^{-4}	4.531×10^{-5}	-3.585×10^{-4}
Model 2		1.993×10^{-4}		6.265×10^{-4}	5.747×10^{-4}		1.505×10^{-4}	-3.010×10^{-4}
Model 3		2.206×10^{-4}		6.841×10^{-4}	5.322×10^{-4}	1.340×10^{-4}	4.531×10^{-5}	-3.585×10^{-4}
Model 4	4.412×10^{-4}		3.068×10^{-6}	6.841×10^{-4}	5.322×10^{-4}	-8.665×10^{-5}	2.659×10^{-4}	-3.585×10^{-4}
Path I′ (W2–W9)								
Model 1	1.497×10^{-5}	-1.702×10^{-5}	1.144×10^{-4}		2.152×10^{-5}	-2.321×10^{-4}	2.145×10^{-4}	3.525×10^{-5}
Model 2	-1.233×10^{-4}	5.212×10^{-5}	1.144×10^{-4}			-1.630×10^{-4}	1.454×10^{-4}	3.525×10^{-5}
Model 3	-1.221×10^{-4}	5.080×10^{-5}	1.144×10^{-4}	2.824×10^{-6}		-1.629×10^{-4}	1.467×10^{-4}	3.242×10^{-5}
Model 4		-1.024×10^{-5}	1.144×10^{-4}	2.824×10^{-6}	2.293×10^{-5}	-2.239×10^{-4}	2.077×10^{-4}	3.242×10^{-5}
Path II′ (W31–W35)								
Model 1		1.425×10^{-4}	1.631×10^{-4}	3.952×10^{-5}	2.310×10^{-4}	-5.416×10^{-5}	3.213×10^{-5}	4.405×10^{-5}
Model 2	-6.427×10^{-5}	1.747×10^{-4}	1.631×10^{-4}	3.952×10^{-5}	2.310×10^{-4}	-2.202×10^{-5}		4.405×10^{-5}
Model 3	-1.083×10^{-4}	1.967×10^{-4}	1.631×10^{-4}	3.952×10^{-5}	2.310×10^{-4}		-2.202×10^{-5}	4.405×10^{-5}
Model 4	2.850×10^{-4}		1.631×10^{-4}	3.952×10^{-5}	2.310×10^{-4}	-1.967×10^{-4}	1.747×10^{-4}	4.405×10^{-5}

Path I was selected to study the hydrogeochemical direction in the northern part of the study area during the late 2010s. At the beginning and end of the simulation path, the saturation indices of calcite and dolomite were greater than 0, indicating a precipitation trend, whereas the saturation indices of gypsum, halite, and CO_2 (g) were less than 0, indicating a dissolution trend. Three simulation models were constructed along this path. In Model 3, the transfer amounts of gypsum and halite dissolution were 4.285×10^{-4} mol/L and 7.283×10^{-4} mol/L, respectively, and a small amount of calcite (4.844×10^{-5} mol/L) was also dissolved. Simultaneously, Ca–Mg and Na–Mg exchanges occurred because Ca^{2+} and Na^{+} were adsorbed by water-bearing media, whereas Mg^{2+} was released into the groundwater. Model 3 reflects the hydrogeochemical process along this path better than the other two models.

Path I′ was selected to analyze the hydrochemical evolution in the northern part of the study area during the 1970s, and four models were output from the hydrogeochemical simulation. Table 3 shows the different states of carbonate minerals in the groundwater along paths I and I′. Dolomite at the beginning and end of path I′ always exhibited a dissolving trend, whereas calcite changed from a slight precipitation trend to an equilibrium state with groundwater. In Model 3, the dissolution amounts of dolomite, gypsum, and halite were 5.080×10^{-5} mol/L, 1.144×10^{-4} mol/L, and 2.824×10^{-6} mol/L, respectively. The dissolution of gypsum and dolomite increased the concentration of Ca^{2+}, which further promoted calcite precipitation and cation exchange processes. The precipitation amount of calcite was 1.221×10^{-4} mol/L and the total transfer amount of Ca^{2+} adsorbed by water-bearing media during Ca–Na and Ca–Mg ion exchange was 1.629×10^{-4} mol/L. Therefore, Model 3 is the most suitable for reflecting the hydrogeochemical evolution along this path. In paths I and I′, although gaseous CO_2 always presented an unsaturated

state with groundwater, CO_2 dissolution in the flow paths was basically not considered. Gaillardet et al. (1999) [71] and Zhong et al. (2018) [72] previously showed that rivers can have a relatively effective reaction surface with CO_2 and that the CO_2 fluxes consumed by carbonate and silicate weathering increase with the increasing river discharge. However, due to limitations in burial and recharge conditions, groundwater often cannot obtain sufficient CO_2 sources. The dissolution of carbonates in paths I and I′ was relatively weak, with the dolomite remaining unsaturated with groundwater at the end point of path I′, which suggests that it may be influenced by inadequate CO_2 sources.

Flow path II is illustrated in Figure 7. It represents the direction of hydrogeochemical evolution in the southern part of the study area in the late 2010s. Similar to path I, calcite and dolomite also showed precipitation trends at the beginning and end points of the path, but the HCO_3^- concentration increased more significantly than that in the other three paths. Therefore, carbonate dissolution must be considered in karst water-bearing media [62]. Merkel and Planer-Friedrich [55] suggested that this continued dissolution trend may be due to the ionic strength effect; that is, when the concentration of ions in groundwater increases, the ionic strength between ions also increases, thus weakening the activity of ions and slowing down the precipitation process. Finally, the dissolution rate of insoluble minerals temporarily exceeds the precipitation rate, reaching an equilibrium in the direction of dissolution. In Model 4, the dissolution of calcite, gypsum, and halite as well as Ca–Mg and Na–Mg ion exchange occurred, which can more comprehensively and accurately describe the ion source and related hydrochemical processes along this path.

Flow path II′ (Figure 8) represents the hydrogeochemical evolution of the southern part of the study area during the 1970s. Compared with that of flow path II, calcite and dolomite showed a dissolution trend at the start point of path II′, with gypsum and halite also more unsaturated. Due to the dilution effect, the concentrations of most ions decrease with increasing water volume [72]. Therefore, the dilution effect may also be one of the reasons why the of main ion concentrations in the 1970s with abundant karst groundwater were lower than those in the 2010s with a significant decrease in groundwater level. At the end point, both calcite and dolomite were approximately in equilibrium with the groundwater. However, none of the four output models indicate the dissolution of both calcite and dolomite but the dissolution of the two minerals alone or the dissolution of dolomite accompanied by the precipitation of calcite. According to the results of previous studies [73,74], the dissolution of gypsum in carbonate formations helps to increase the concentration ratio of Ca^{2+} and Mg^{2+} while providing SO_4^{2-}, both of which promote the dedolomitization process. The main reaction of dedolomitization can be expressed as follows (aq. refers to dissolved species, and s refers to solid):

$$CaMg(CO_3)_2\ (s) + Ca^{2+}\ (aq.) + SO_4^{2-}\ (aq.) \rightarrow 2CaCO_3\ (s) + Mg^{2+}\ (aq.) + SO_4^{2-}\ (aq.), \quad (5)$$

The reaction stops when the groundwater is saturated with dolomite and calcite [75]. In path II′, Model 2 indicates the dissolution of dolomite and precipitation of a small amount of calcite until the two minerals are in equilibrium with the groundwater. In addition, common Ca–Na ion exchange occurs, which increases Na^+ concentration in the groundwater. Therefore, Model 2 best reflects the hydrochemical evolution along this path.

5. Conclusions

To assess the hydrochemical response of karst groundwater during urbanization, a field hydrogeological survey was conducted, and groundwater samples from the 2010s and 1970s were analyzed through statistical analysis, hydrochemical diagrams, and inverse simulation technology. The main conclusions can be summarized as follows:

1. The karst groundwater in the study area is freshwater. Its alkalinity slightly increased in recent years. The TDS and TH values significantly increased, and the TH, NO_3^-, and Fe concentrations exceeded the standard limits. In contrast, these indicators did not exceed the relevant standards during the 1970s.

2. Based on Piper and Stiff diagrams, hydrochemical types in the 1970s mainly included HCO_3-Ca and HCO_3-Ca·Mg, whereas recent water samples show a significant decrease in HCO_3-Ca types as well as the appearance of SO_4·HCO_3-Ca·Mg, HCO_3·Cl-Ca·Mg, HCO_3·Cl·SO_4-Ca·Mg, and HCO_3·SO_4-Ca. Complex hydrochemical types are mainly distributed in the groundwater discharge areas around downtown Xingtai.
3. Person's correlation analysis and contour maps of concentration increments showed that abnormal concentrations of TDS, TH, SO_4^{2-}, NO_3^-, and Cl^- in karst groundwater can be attributed to anthropogenic sources such as sewage and fertilizer. The most significant areas affected by human activities are the two groundwater discharge areas north and south of the center of Xingtai City and Yangfan Town in the south of the study area.
4. According to the cluster analysis as well as Schoeller and scatter diagrams, the 61 water samples from the late 2010s were divided into three groups. Groups 1 and 2 included water samples with low and gradually increasing concentrations, respectively, from the recharge–runoff area and the linkage distance between the two groups was relatively close. Water samples that were significantly affected by human activities, such as those near the discharge area, were clustered in Group 3. The clustering results indicated similar sources and hydrochemical evolution processes for the water samples within the group.
5. Inverse hydrogeochemical models showed that the dissolution of gypsum and halite, as well as cation exchange, occurs during the flow of karst groundwater in water-bearing media. Compared with the recent period, dolomite and calcite mostly dissolved during the 1970s or dedolomitization occurred. Because of the overall increase in ion concentrations in recent years, the dissolution trend of carbonates has weakened; however, the effect of the ionic strength has increased, allowing carbonate minerals to continue to dissolve, further increasing ion concentrations along the flow path.

Based on current findings, it is necessary to implement strict groundwater management policies for urban sewage discharge and fertilizer application in agricultural practices. To minimize the negative impacts of human activities, further research into the prediction of hydrochemical compositions under varying degrees of human activity and corresponding management measures is warranted. Meanwhile, continuous monitoring and analysis of abnormal areas are also recommended.

Author Contributions: Conceptualization, X.L. and R.W.; methodology, R.W.; software, R.W., Z.C. and L.S.; validation, R.W. and F.D.; formal analysis, W.H. and Z.J.; investigation, X.L. and W.H.; resources, X.L.; data curation, X.L.; writing—original draft preparation, R.W.; writing—review and editing, X.L. and F.D.; visualization, X.L. and Z.C.; supervision, X.L.; project administration, X.L. and R.W.; funding acquisition, X.L., R.W. and F.D. All authors have read and agreed to the published version of the manuscript.

Funding: This research was financially supported by the Special Fund for Basic Scientific Research of Chinese Academy of Geological Sciences (JYYWF20181301), the S&T Program of Hebei (D2019403193, 22373601D), and the Youth Science and Technology Foundation of Hebei GEO University (QN202111).

Data Availability Statement: Data available on request from the corresponding author.

Acknowledgments: The authors are very grateful to the Hebei Center for Ecological and Environmental Geology Research for the technical support of this study, as well as to the anonymous reviewers and editors of the paper.

Conflicts of Interest: The authors declare no conflict of interest.

References

1. Xu, H.Z.; Jiao, M. City size, industrial structure and urbanization quality—A case study of the Yangtze River Delta urban agglomeration in China. *Land Use Policy* **2021**, *111*, 105735. [CrossRef]
2. Li, X.Y.; Zhang, Y.L.; Li, Z.H.; Wang, R. Response of the groundwater environment to rapid urbanization in Hohhot, the provincial capital of western China. *J. Hydrol.* **2021**, *603*, 127033. [CrossRef]

3. Population Division, Department of Economic and Social Affairs, United Nations. World Urbanization Prospects: The 2018 Revision. Available online: httpis://www.un.org/zh/desa/2018-revision-world-urbanization-prospects (accessed on 16 May 2018).
4. The China State Council. *Major Figures on 2020 Population Census of China*; China Statistics Press: Beijing, China, 2021; pp. 3–39.
5. Yang, S.Y. The Impact of urbanization on the temporal and spatial evolution of air quality: A case study of Hubei Province. *Curr. Urban Stud.* **2021**, *9*, 659–676. [CrossRef]
6. Leeson, G.W. The growth, ageing and urbanisation of our World. *J. Popul. Ageing* **2018**, *11*, 107–115. [CrossRef]
7. Wu, J.S.; Cheng, D.J.; Xu, Y.Y.; Huang, Q.; Feng, Z. Spatial-temporal change of ecosystem health across China: Urbanization impact perspective. *J. Clean. Prod.* **2021**, *326*, 129393. [CrossRef]
8. Gross, J.; Ouyang, Y. Types of urbanization and economic growth. *Int. J. Urban. Sci.* **2021**, *25*, 71–85. [CrossRef]
9. Atack, J.; Margo, R.A.; Rhode, P.W. Industrialization and urbanization in nineteenth century America. *Reg. Sci. Urban. Econ.* **2022**, *94*, 103678. [CrossRef]
10. Zhang, J.J.; Zhou, T.G. Coupling coordination degree between ecological environment quality and urban development in Chengdu–Chongqing economic circle based on the Google Earth Engine platform. *Sustainability* **2023**, *15*, 4389. [CrossRef]
11. Ariken, M.; Zhang, F.; Liu, K.; Fang, C.; Kung, H.-T. Coupling coordination analysis of urbanization and eco-environment in Yanqi Basin based on multi-source remote sensing data. *Ecol. Indic.* **2020**, *114*, 106331. [CrossRef]
12. Xu, Z.Q.; Xiao, S.H.; Du, C.; Deng, Q.Y.; Yan, B.F.; Zeng, Z.W.; Liu, X.Y. Temporal variation of water environment carrying capacity in a highly urbanized region of China. *Water* **2020**, *12*, 3362. [CrossRef]
13. Masoud, A.A.; Koike, K.; Mashaly, H.A.; Gergis, F. Spatio-temporal trends and change factors of groundwater quality in an arid area with peat rich aquifers: Emergence of water environmental problems in Tanta District, Egypt. *J. Arid Environ.* **2016**, *124*, 360–376. [CrossRef]
14. Nakayama, T.; Wang, Q.X.; Okadera, T. Evaluation of spatio-temporal variations in water availability using a process-based eco-hydrology model in arid and semi-arid regions of Mongolia. *Ecol. Model.* **2021**, *440*, 109404. [CrossRef]
15. Mashhadi Ali, A.; Shafiee, M.E.; Berglund, E.Z. Agent-based modeling to simulate the dynamics of urban water supply: Climate, population growth, and water shortages. *Sustain. Cities Soc.* **2017**, *28*, 420–434. [CrossRef]
16. Zhou, Q.; Leng, G.; Su, J.; Ren, Y. Comparison of urbanization and climate change impacts on urban flood volumes: Importance of urban planning and drainage adaptation. *Sci. Total Environ.* **2019**, *658*, 24–33. [CrossRef] [PubMed]
17. Ahani, S.; Dadashpoor, H. A review of domains, approaches, methods and indicators in peri-urbanization literature. *Habitat Int.* **2021**, *114*, 102387. [CrossRef]
18. Wang, X.J.; Wang, D.Y.; Wu, S.Z.; Yan, Z.R.; Han, J.Q. Cultivated land multifunctionality in undeveloped peri-urban agriculture areas in China: Implications for sustainable land management. *J. Environ. Manag.* **2023**, *325*, 116500. [CrossRef]
19. Masoud, A.A.; El-Horiny, M.M.; Arafa, N.A.A.-W.; El-Bouraie, M. Environmental factors impacting the disparity rate in hydrochemical pollution under industrial urban centers and intensified agriculture. *Int. J. Environ. Sci. Technol.* **2022**, *19*, 7181–7204. [CrossRef]
20. Maghrebi, M.; Noori, R.; Partani, S.; Araghi, A.; Barati, R.; Farnoush, H.; Haghighi, A.T. Iran's groundwater hydrochemistry. *Earth Space Sci.* **2021**, *8*, e2021EA001793. [CrossRef]
21. Carey, R.O.; Hochmuth, G.J.; Martinez, C.J.; Boyer, T.H.; Nair, V.D.; Dukes, M.D.; Toor, G.S.; Shober, A.L.; Cisar, J.L.; Trenholm, L.E.; et al. A review of turfgrass fertilizer management practices: Implications for urban water quality. *HortTechnology* **2012**, *22*, 280–291. [CrossRef]
22. Karunanidhi, D.; Aravinthasamy, P.; Deepali, M.; Subramani, T.; Bellows, B.C.; Li, P.Y. Groundwater quality evolution based on geochemical modeling and aptness testing for ingestion using entropy water quality and total hazard indexes in an urban-industrial area (Tiruppur) of Southern India. *Environ. Sci. Pollut. Res.* **2021**, *28*, 18523–18538. [CrossRef]
23. Huang, G.X.; Zhang, M.; Liu, C.Y.; Li, L.P.; Chen, Z.Y. Heavy metal(loid)s and organic contaminants in groundwater in the Pearl River Delta that has undergone three decades of urbanization and industrialization: Distributions, sources, and driving forces. *Sci. Total Environ.* **2018**, *635*, 913–925. [CrossRef]
24. Maghrebi, M.; Noori, R.; AghaKouchak, A. Iran: Renovated irrigation network deepens water crisis. *Nature* **2023**, *618*, 238. [CrossRef]
25. Carlson, M.A.; Lohse, K.A.; McIntosh, J.C.; McLain, J.E.T. Impacts of urbanization on groundwater quality and recharge in a semi-arid alluvial basin. *J. Hydrol.* **2011**, *409*, 196–211. [CrossRef]
26. Banerjee, S.; Sikdar, P.K. Hydrogeological characterization of the Quaternary aquifer of south Bengal Basin in India and the impact of urbanization on the groundwater resources of the system. *Hydrogeol. J.* **2021**, *29*, 1463–1484. [CrossRef]
27. Ahmed, M.; Chen, Y.; Khalil, M.M. Isotopic composition of groundwater resources in arid environments. *J. Hydrol.* **2022**, *609*, 127773. [CrossRef]
28. Nunes, K.G.; Costa, R.N.T.; Cavalcante, I.N.; Gondim, R.S.; Lima, S.C.R.V.; Mateos, L. Groundwater resources for agricultural purposes in the Brazilian semi-arid region. *Rev. Bras. Eng. Agr. Amb.* **2022**, *26*, 915–923. [CrossRef]
29. Wakode, H.B.; Baier, K.; Jha, R. Impact of urbanization on groundwater recharge and urban water balance for the city of Hyderabad, India. *Int. Soil Water Conse.* **2018**, *6*, 51–62. [CrossRef]
30. Haq, F.; Naeem, U.A.; Gabriel, H.F.; Khan, N.M.; Ahmad, I.; Rehman, H.U.; Zafar, M.A. Impact of urbanization on groundwater levels in Rawalpindi City, Pakistan. *Pure Appl. Geophys.* **2021**, *178*, 491–500. [CrossRef]

31. Yin, S.X.; Han, Y.; Zhang, Y.S.; Zhang, J.C. Depletion control and analysis for groundwater protection and sustainability in the Xingtai region of China. *Environ. Earth Sci.* **2016**, *75*, 1246. [CrossRef]
32. Cao, R.J.; Jiang, R.G.; Zhao, Y.; Xie, J.C.; Yu, X. Spatiotemporal characteristics of groundwater depth in Xingtai City on the North China Plain: Changing patterns, causes and prediction. *Appl. Ecol. Env. Res.* **2020**, *18*, 6605–6622. [CrossRef]
33. Shi, H.R.; Huang, X.N.; Xu, S.; Hao, J.F. Climate change in Xingtai City in recent 56 years and its impact on climate productivity. *Meteor. Environ. Res.* **2019**, *10*, 102–103.
34. Liu, Y.X.; Liang, Y.; Qiao, L. Analysis on water-rock reaction characteristics of groundwater system in Xingtai-Baiquan springs. *S. N. Water Transf. Water Sci. Technol.* **2009**, *7*, 63–66, (In Chinese with English abstract).
35. Zhao, X.W.; Wu, L.; Han, X. Division of karst water protection areas based on analysis of hydrogeologic conditions. *Carsologica Sin.* **2017**, *36*, 526–532, (In Chinese with English abstract).
36. The Second Geological Bureau of Hydrogeology and Engineering Geology of Hebei Province, China. *Report on Hydrogeological Survey of the Southern Section of the Taihang Mountain, People's Republic of China*; Hebei Bureau of Geology and Mineral Resources Exploration: Shijiazhuang, China, 1991; pp. 44–89.
37. Li, X.H.; Xu, S.J.; Zhang, Z.P.; Liu, Z. *Special Research Report on Ecological Protection and Restoration Countermeasures of Baiquan Spring Region in Xingtai City*; Institute of Hydrogeology and Environmental Geology, Chinese Academy of Geological Sciences (CAGS): Shijiazhuang, China, 2019; pp. 6–38.
38. Wang, J.A.; Shang, X.C.; Ma, H.T. Investigation of catastrophic ground collapse in Xingtai gypsum mines in China. *Int. J. Rock Mech. Min.* **2008**, *45*, 1480–1499. [CrossRef]
39. Wang, H.Y.; Yuan, Z.M. Karst groundwater systems in Xingtai area, Hebei province. *Hydrogeol. Eng. Geol.* **1990**, *6*, 14–18, (In Chinese with English abstract)
40. Qiao, G.J. Study on feasibility of restoring spring water quantity at Baiquan of Xingtai City. *Water Resour. Prot.* **2006**, *22*, 46–49, 52, (In Chinese with English abstract).
41. Liang, Y.P.; Gao, X.B.; Zhao, C.H.; Tang, C.L.; Shen, H.Y.; Wang, Z.H.; Wang, Y.X. Review: Characterization, evolution, and environmental issues of karst water systems in Northern China. *Hydrogeol. J.* **2018**, *26*, 1371–1385. [CrossRef]
42. Wang, R.; Li, X.H.; Wei, A.H. Hydrogeochemical characteristics and gradual changes of groundwater in the Baiquan karst spring region, northern China. *Carbonates Evaporites* **2022**, *37*, 47. [CrossRef]
43. Ministry of Environmental Protection of the People's Republic of China. *Technical Specifications for Environmental Monitoring of Groundwater (HJ/T164–2004)*; Standards Press of China: Beijing, China, 2004; pp. 7–48.
44. Yetiş, R.; Atasoy, A.D.; Demir Yetiş, A.; Yeşilnacar, M.İ. Hydrogeochemical characteristics and quality assessment of groundwater in Balikligol Basin, Sanliurfa, Turkey. *Environ. Earth Sci.* **2019**, *78*, 331. [CrossRef]
45. Singh, A.K.; Mondal, G.C.; Singh, T.B.; Singh, S.; Tewary, B.K.; Sinha, A. Hydrogeochemical processes and quality assessment of groundwater in Dumka and Jamtara districts, Jharkhand, India. *Environ. Earth Sci.* **2012**, *67*, 2175–2191. [CrossRef]
46. Wei, A.H.; Chen, Y.Y.; Deng, Q.H.; Li, D.; Wang, R.; Jiao, Z. A Study on hydrochemical characteristics and evolution processes of groundwater in the coastal area of the Dagujia River Basin, China. *Sustainability* **2022**, *14*, 8358. [CrossRef]
47. Pisciotta, A.; Tiwari, A.K.; Maio, M.D. An integrated multivariate statistical analysis and hydrogeochemical approaches to identify the major factors governing the chemistry of water resources in a mountain region of northwest Italy. *Carbonates Evaporites* **2019**, *34*, 955–973. [CrossRef]
48. Helstrup, T.; Jørgensen, N.O.; Banoeng-Yakubo, B. Investigation of hydrochemical characteristics of groundwater from the Cretaceous-Eocene limestone aquifer in southern Ghana and southern Togo using hierarchical cluster analysis. *Hydrogeol. J.* **2007**, *15*, 977–989. [CrossRef]
49. IBM SPSS Statistics 21.0. Available online: https://www.ibm.com/support/pages/release-notes-ibm-spss-statistics-210 (accessed on 17 June 2018).
50. Piper, A.M. A graphical interpretation of water-analysis. *Trans. Am. Geophys. Union* **1944**, *25*, 914–928. [CrossRef]
51. Stiff, H.A. The interpretation of chemical water analysis by means of patterns. *J. Pet. Technol.* **1951**, *3*, 15. [CrossRef]
52. Lee, B.D.; Jeong, C.H.; Lee, Y.C.; Lee, Y.J.; Yang, J.H.; Choo, C.O.; Jang, H.W.; Oh, Y.H.; Hong, J.W. Statistical analysis and thermodynamic equilibrium modelling for chemical composition of groundwater and spring water at Jeju Island, South Korea. *Water* **2022**, *12*, 777. [CrossRef]
53. Khan, M.; Almazah, M.M.A.; EIlahi, A.; Niaz, R.; Al-Rezami, A.Y.; Zaman, B. Spatial interpolation of water quality index based on Ordinary kriging and Universal kriging. *Geomat. Nat. Haz. Risk* **2023**, *14*, 2190853. [CrossRef]
54. Zhang, B.; Zhao, D.; Zhou, P.P.; Qu, S.; Liao, F.; Wang, G.C. Hydrochemical characteristics of groundwater and dominant water–rock interactions in the Delingha area, Qaidam Basin, Northwest China. *Water* **2020**, *12*, 836. [CrossRef]
55. Merkel, B.J.; Planer-Friedrich, B. *Groundwater Geochemistry—A Practical Guide to Modeling of Natural and Contaminated Aquatic Systems*; Springer: Berlin, Germany, 2005; pp. 20–110.
56. Ravikumar, P.; Somashekar, R.K. Principal component analysis and hydrochemical facies characterization to evaluate groundwater quality in Varahi river basin, Karnataka state, India. *Appl. Water Sci.* **2017**, *7*, 745–755. [CrossRef]
57. Li, Y.Z.; Liu, J.T.; Gao, Z.J.; Wang, M.; Yu, L.Q. Major ion chemistry and water quality assessment of groundwater in the Shigaze urban area, Qinghai-Tibetan Plateau, China. *Water Supply* **2020**, *20*, 335–347. [CrossRef]
58. General Administration of Quality Supervision, Inspection and Quarantine of the People's Republic of China. *Standard for Groundwater Quality*; Standards Press of China: Beijing, China, 2017; pp. 2–6.

59. World Health Organization. *Guidelines for Drinking Water Quality*, 4th ed.; WHO Press: Geneva, Switzerland, 2011; pp. 307–433.
60. Henson, W.R.; Huang, L.; Graham, W.D.; Ogram, A. Nitrate reduction mechanisms and rates in an unconfined eogenetic karst aquifer in two sites with different redox potential. *J. Geophys. Res. Biogeo.* **2017**, *122*, 1062–1077. [CrossRef]
61. Zheng, W.B.; Wang, S.Q. Extreme precipitation accelerates the contribution of nitrate sources from anthropogenetic activities to groundwater in a typical headwater area of the North China Plain. *J. Hydrol.* **2021**, *603*, 127110. [CrossRef]
62. Shukla, S.; Saxena, A.; Khan, R.; Li, P. Spatial analysis of groundwater quality and human health risk assessment in parts of Raebareli district, India. *Environ. Earth Sci.* **2021**, *80*, 800. [CrossRef]
63. Li, P.Y.; Tian, R.; Liu, R. Solute geochemistry and multivariate analysis of water quality in the Guohua phosphorite mine, Guizhou Province, China. *Expos. Health* **2019**, *11*, 81–94. [CrossRef]
64. Squillace, P.J.; Moran, M.J. Factors associated with sources, transport, and fate of volatile organic compounds and their mixtures in aquifers of the United States. *Environ. Sci. Technol.* **2007**, *41*, 2123–2130. [CrossRef] [PubMed]
65. Yidana, S.M. Groundwater classification using multivariate statistical methods: Birimian Basin, Ghana. *J. Environ. Eng.* **2010**, *136*, 1379–1388. [CrossRef]
66. Omo-Irabor, O.O.; Olobaniyi, S.B.; Oduyemi, K.; Akunna, J. Surface and groundwater water quality assessment using multivariate analytical methods: A case study of the Western Niger Delta, Nigeria. *Phys. Chem. Earth* **2008**, *33*, 666–673. [CrossRef]
67. Rusi, S.; Curzio, D.D.; Palmucci, W.; Petaccia, R. Detection of the natural origin hydrocarbon contamination in carbonate aquifers (central Apennine, Italy). *Environ. Sci. Pollut. R.* **2018**, *25*, 15577–15596. [CrossRef]
68. Guo, Y.L.; Zhang, C.; Xiao, Q.; Bu, H. Hydrogeochemical characteristics of a closed karst groundwater basin in North China. *J. Radioanal. Nucl. Chem.* **2020**, *325*, 365–379. [CrossRef]
69. Zhong, J.; Li, S.-L.; Ibarra, D.E.; Ding, H.; Liu, C.-Q. Solute production and transport processes in Chinese monsoonal rivers: Implications for global climate change. *Glob. Biogeochem. Cycles* **2020**, *34*, e2020GB006541. [CrossRef]
70. Jia, Z.X.; Zang, H.F.; Hobbs, P.; Zheng, X.Q.; Xu, Y.X.; Wang, K. Application of inverse modeling in a study of the hydrogeochemical evolution of karst groundwater in the Jinci Spring region, northern China. *Environ. Earth Sci.* **2017**, *76*, 312. [CrossRef]
71. Gaillardet, J.; Dupré, B.; Louvat, P.; Allegrè, C.J. Global silicate weathering and CO_2 consumption rates deduced from the chemistry of large rivers. *Chem. Geol.* **1999**, *159*, 3–30. [CrossRef]
72. Zhong, J.; Li, S.-L.; Liu, J.; Ding, H.; Sun, X.L.; Xu, S.; Wang, T.J.; Ellam, R.M.; Liu, C.-Q. Climate variability controls on CO_2 consumption fluxes and carbon dynamics for monsoonal rivers: Evidence from Xijiang River, Southwest China. *J. Geophys. Res. Biogeo.* **2018**, *123*, 2553–2567. [CrossRef]
73. Evamy, B.D. Dedolomitization and the development of rhombohedral pores in limestones. *J. Sediment. Petrol.* **1967**, *37*, 1204–1215. [CrossRef]
74. Houatmia, F.; Azouzi, R.; Charef, A.; Bédir, M. Assessment of groundwater quality for irrigation and drinking purposes and identification of hydrogeochemical mechanisms evolution in Northeastern, Tunisia. *Environ. Earth Sci.* **2016**, *75*, 746. [CrossRef]
75. Boni, M.; Mondillo, N.; Balassone, G. Zincian dolomite: A peculiar dedolomitization case? *Geology* **2011**, *39*, 183–186. [CrossRef]